ACS APPLIED ENERGY MATERIALS

www.acsaem.org Article

Anisotropy of Microstructure and Its Influence on Thermoelectricity: The Case of $Cu_2Te-Sb_2Te_3$ Eutectic

Shriparna Mukherjee,*,# Shanmukha Kiran Aramanda,# Surafel Shiferaw Legese, Alexander Riss, Gerda Rogl, Olu Emmanuel Femi, Ernst Bauer, Peter Franz Rogl, and Kamanio Chattopadhyay*

Cite This: *ACS Appl. Energy Mater.* 2021, 4, 11867−11877 Read Online

ACCESS | Metrics & More | Article Recommendations | Supporting Information

ABSTRACT: Using a set of controlled in situ grown lamellar composites of $(Cu_2Te)_{62.02}-(Sb_2Te_3)_{37.98}$, we report a remarkable variation of transport properties of thermoelectricity not only as a function of microstructural length scale but also as a function of direction-dependent arrangement of the phases and hence their interfaces. A quantitative evaluation of the microstructure along the transverse and the longitudinal directions of growth, imposed by the temperature gradient and growth rate in a unidirectional solidification setup, has been carried out. The microstructure is quantified through image analysis using fast Fourier transforms as well as a cluster base connectivity model and is further correlated with the thermoelectric transport properties. A marked anisotropy of properties as a function of measurement direction in the microstructural landscape could be observed. A maximum power factor of ∼1.4 mW m^{-1} K^{-2} and a figure of merit of 0.29 could be obtained at 580 K along the transverse direction for the sample with the characteristic microstructural length scale of 2.41 μm. This has an implication in engineering a thermoelectric device in terms of engineering power factor and output power density. For a ΔT of 250 K, we report a difference of 0.4 W cm^{-2} in output power density between the transverse and the longitudinal directions that have an identical microstructural length scale of 2.41 μm.

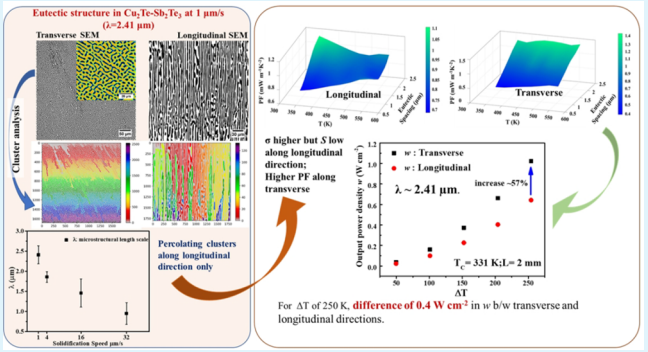

KEYWORDS: *thermoelectric, directional solidification, eutectic, microstructure, transport properties*

1. INTRODUCTION

Microstructure preponderantly influences the thermoelectric properties of materials.[1−7] Some of the strategies for modifying the microstructure for tuning these properties are solidification,[8,9] spinodal decomposition,[1,10,11] and solid-state precipitations.[12−15] Solidification can produce a wide range of microstructural features, from amorphous to multiphase to single crystal during liquid to solid transformation. The temperature gradient across the solid−liquid interface and its growth velocity are the two important processing parameters during solidification that influence the evolution of the microstructure.[16,17] Microstructural modifications through the cooling rate control to enhance the thermoelectric performance have gained attention in the recent past;[18−20] however, these efforts are geared toward reducing the contribution of the lattice thermal conductivity to the total thermal conductivity (κ) to enhance the thermoelectric figure of merit zT (where $zT = S^2\sigma T/\kappa$). The enhancement of the thermoelectric power factor ($S^2\sigma$, where S is the Seebeck coefficient and σ is the electrical conductivity) can also significantly improve the thermoelectric performance that may be equally important to that of the reduction of thermal conductivity.[21−23]

Eutectics are a common feature in many phase diagrams and are utilized for various applications.[5,9,23−32] During the solidification of eutectic systems,[33,34] multiple phases self-organize into characteristic spacings based on the solidification velocity and growth along the imposed temperature gradient. Such alignment of the eutectic phases can exhibit anisotropy of the microstructure and hence the directional dependence of the properties, including thermoelectric transport properties. These have motivated the present study.

The $Cu_2Te-Sb_2Te_3$ pseudobinary phase diagram[35] shown in Figure S1 exhibits a eutectic reaction. A composition $(Cu_2Te)_{62.02}-(Sb_2Te_3)_{37.98}$ of the eutectic alloy was chosen for the present study. In earlier reports, the thermoelectric transport properties of the constituent phases, that is, Cu_2Te and Sb_2Te_3, have been tuned by controlling the charge carrier concentration via doping/alloying[36−39] and by microstructural

Received: August 30, 2021
Accepted: October 4, 2021
Published: October 14, 2021

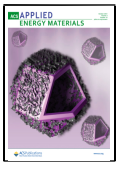

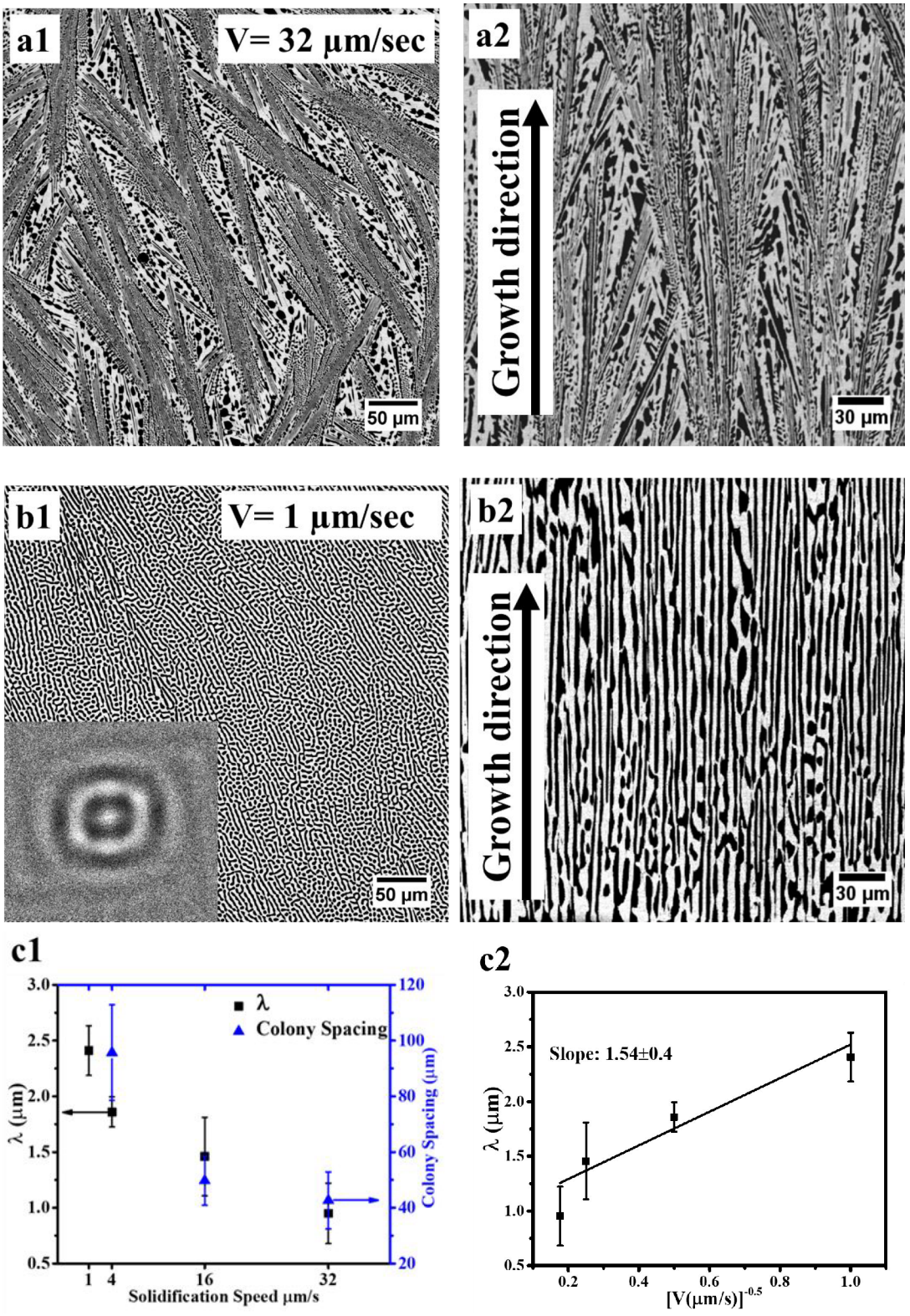

Figure 1. (a1,a2 and b1,b2) Micrographs captured from directionally solidified samples for 32 and 1 μm/s, respectively; (a1) and (b1) are micrographs along the transverse direction, while (a2) and (b2) are micrographs along the longitudinal direction. The inset in (b1) shows the FFT of the image. (c1) Variation of microstructural length scale (λ) and colony spacing with different solidification velocities and (c2) variation of λ with the inverse square root of different solidification velocities.

engineering.[40,41] Both chalcogenides crystallize with a trigonal crystal structure and are intrinsically p-type semiconductors that form a solid solution with each other over a wide range of compositions. Cu_2Te has unique electronic properties[42] and belongs to the phonon-liquid-electron-crystal (PLEC) system possessing low thermal conductivity.[43,44] Sb_2Te_3 is a room-temperature thermoelectric material used mostly for refrigeration applications.[45] A qualitative study of a set of Cu_2Te–

https://doi.org/10.1021/acsaem.1c02664
ACS Appl. Energy Mater. 2021, 4, 11867−11877

Sb_2Te_3 pseudobinary alloys along with their microstructure and thermoelectric properties is available.[40] However, very few studies in the literature aim to correlate the microstructural length scale and arrangements of multicomponent phases quantitatively with the thermoelectric power factor. This study aims to achieve this through directional solidification using a modified-Bridgman-type apparatus (shown in Figure S2).

2. EXPERIMENTAL SECTION

The pseudobinary eutectic alloy composition $(Cu_2Te)_{62.02}$–$(Sb_2Te_3)_{37.98}$ was chosen for the present study following the phase diagram given in Figure S1.[35] The elemental shots of Cu (4N), Sb (4N), and Te (4N) were weighed according to the stoichiometric ratio of Cu (33 at. %), Sb (20.21 at. %), and Te (46.79 at. %) and sealed in evacuated quartz tubes. The elemental mixtures were induction melted to obtain a homogeneous composition. The synthesized alloy was subsequently sealed in evacuated quartz tubes for directional solidification experiments. A modified-Bridgman apparatus was used for directionally solidifying the alloys. The details of the apparatus are given below.

2.1. Description of the Apparatus. The modified-Bridgman-type apparatus consists of an isothermal hot zone and an isothermal chill zone separated by an insulating zone, as shown in Figure S2a. The required temperature of the hot zone is achieved through resistance heating (Kanthal-A is used as a heating element). The chill zone at a lower temperature is maintained by continuous circulation of cold water. The purpose of the insulation zone is to establish a thermal gradient between the hot and chill zones without much heat transfer between the zones. The axial temperature profile in the apparatus is obtained when the hot zone is set at 923 K, while the chill zone is kept at 398 K through water circulation. The temperatures were measured using a thermocouple kept stationary while the furnace is moved relative to the thermocouple. The axial temperature plot is shown in Figure S2b. The temperature gradient at the melting point of the eutectic is calculated using the axial temperature plot and is 23.4 K/mm. More details about the apparatus are given in refs 46 and 47. We have varied the solidification rates by changing the apparatus' traverse rate relative to the stationary sample using a gearbox coupled with a linear drive. Using this assembly, we could directionally solidify the alloys up to a length of 80 mm at a constant temperature gradient (23.4 K/mm) with variable pull velocities (V = 1, 4, 16, and 32 μm/s). An image of a typical sample is shown in Figure S2c.

2.2. Characterization Techniques. Traditional polishing techniques were employed for metallographic analysis of transverse and longitudinal sections of the directionally solidified samples. Microstructure characterization has been carried out using a field-emission tip equipped electron probe microanalyzer (JEOL, JXA-8530F). Cylindrical samples of ca. 12 mm × 6 mm were used to measure the transport properties, both parallel and perpendicular to the solidification direction as shown in Figure S3a and b, respectively. The transport properties such as the Seebeck coefficient and electrical resistivity of the alloys were measured in the temperature range between 300 and 600 K, using a ULVAC ZEM-3 system. A differential method was used to measure the Seebeck coefficient, while a four-probe method was used for electrical resistivity. The errors in measurement for the Seebeck coefficient and electrical resistivity were 7% and 10%, respectively. The thermal diffusivity (D) was measured with the laser flash method, using LINSEIS LFA 500 equipment. For the measurements, discs with a diameter of 6 mm and a height of 1 mm or square-shaped plates with a dimension of 6 mm × 6 mm × 1 mm were used. The diffusivity was measured from 300 to 600 K in steps of 20 K, using four laser-shots for each temperature point. The thermal conductivity, κ, was calculated according to the relation $\kappa = D \times C_p \times \rho$, with ρ as the measured density of the sample. Here, we have taken the Dulong Petit value for the specific heat capacity (C_p) for ease of calculations. We have also measured the temperature-dependent C_p using LINSEIS DSC-PT10 equipment, and the results have been included in Figure S12.

3. RESULTS AND DISCUSSION

3.1. Microstructure and Phase Analysis. Microstructures along both parallel as well as perpendicular to the solidification direction were characterized using a field-emission scanning electron microscope (SEM) and are presented in Figure 1 for different solid–liquid interfacial velocities. The microstructures of the transverse sections are shown at lower magnification in Figure 1a1 and b1 and in Figure S4. The features at higher magnification are revealed in Figure S5. Figure 1a2 and b2 shows the micrographs of the longitudinal sections. The microstructures reveal the formation of two-phase colonies in the samples solidified at a growth velocity (V) of 32, 16, and 4 μm/s. The alloys chosen for the study fall in the pseudobinary eutectic valley of the ternary phase diagram[35] and can undergo a univariant eutectic reaction during solidification. Depending on the growth conditions, instabilities can develop beyond a critical velocity leading to the formation of a two-phase colony. This phenomenon is very similar to the Mullins–Sekerka instability[48] that occurs in single-phase solidification and is reported in the literature.[46,49,50] At velocities greater than 1 μm/s, the eutectic front, in the present case, gets destabilized, which causes the formation of these colonies.

3.1.1. Morphology and Eutectic Length Scale Selection. The growth direction of the eutectics is along $[10\bar{1}0]$ of trigonal Cu_2Te as shown in Figure S6. The morphology of the eutectic is complex lamellar inside the colony at higher velocities, that is, V = 32, 16 μm/s; however, with a decrease in velocity to 4 and 1 μm/s, we predominantly observe a degenerate morphology of the eutectic. The morphology of the colonies in all cases is plate-like. The determination of the characteristic length scale of these microstructures is not straightforward. We have determined the length scale of the complex arrangement of the two phases in the microstructure by digitizing the image and carrying out fast Fourier transformation (FFT) as shown in the inset of Figure 1b1 (details in Figure S7). The colony spacings were measured by the line intercept method using ImageJ software and are presented in Table 1 and Figure 1c1 as a function of growth velocity. Eutectic scaling (λ, i.e., microstructural length scale), according to the Jackson Hunt theory,[51] follows the $\lambda^2 V$ = constant (V is the velocity of the solid–liquid interface). The variation of the characteristic microstructural length scale (λ) between the two phases has been plotted against the inverse square root of velocity ($V^{-0.5}$) in Figure 1c2. The microstructural length scale of the eutectic shows an increasing trend with a decrease in velocity. The square of the slope of the linear fit gives the scaling constant $\lambda^2 V$ as ca. 1.54 ± 0.4 $\mu m^3/s$. A slight deviation from the linear fit could be due to the formation of colonies in the eutectic system.

Table 1. Microstructural Length Scale from FFT (λ) and Colony Spacing of the Alloys at Different Solidification Rates

nomenclature	solidification rate (μm/s)	λ (μm)	colony spacing (μm)
alloy 1	1	2.41 ± 0.22	∞
alloy 2	4	1.86 ± 0.13	95.7 ± 17.2
alloy 3	16	1.46 ± 0.35	49.7 ± 8.8
alloy 4	32	0.95 ± 0.27	42.7 ± 10.2

https://doi.org/10.1021/acsaem.1c02664
ACS Appl. Energy Mater. 2021, 4, 11867–11877

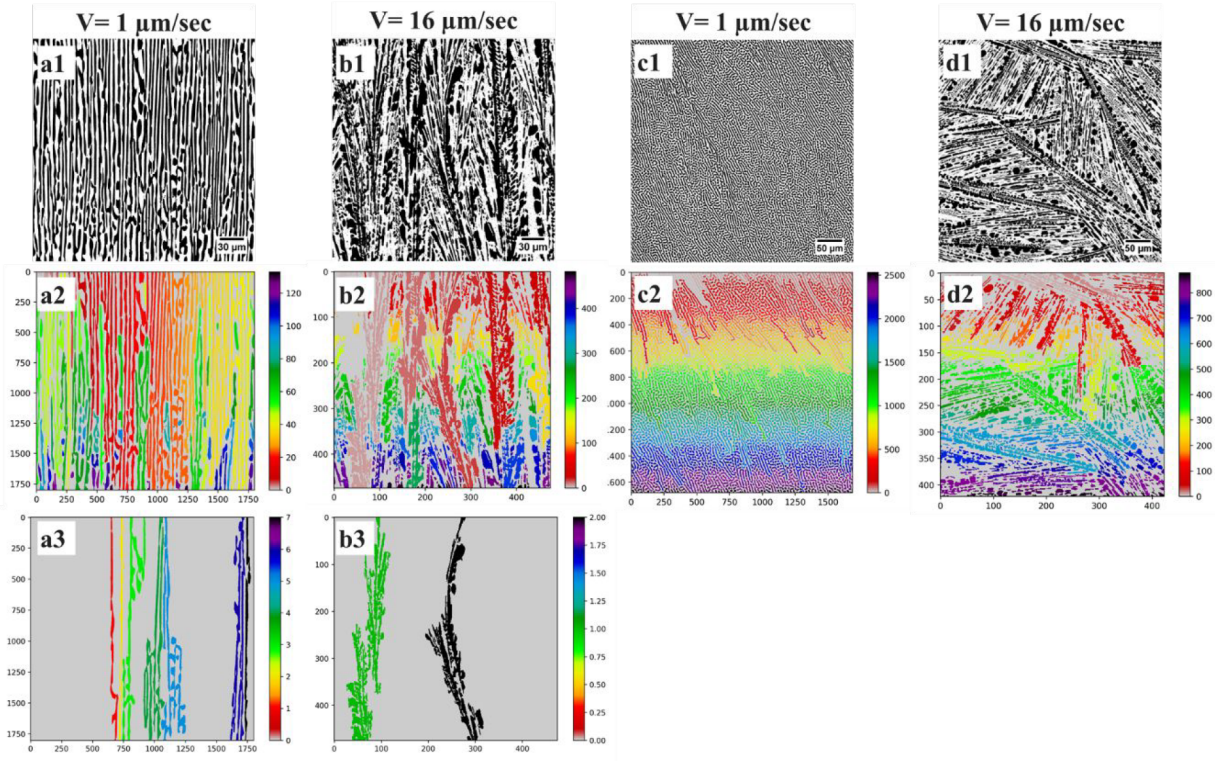

Figure 2. Quantitative analysis of micrographs of samples solidified at 1 μm/s shown in (a) and (c) and at 16 μm/s shown in (b) and (d); (a) and (b) are along the longitudinal section, while (c) and (d) are along the transverse section. The number of clusters in each image is shown below its SEM image (refer to a2, b2, c2, and d2), where each cluster has an identity with a unique color, as shown in the legend. Percolating clusters corresponding to longitudinal sections are shown in (a3) and (b3), whereas transverse sections do not have any percolating clusters in both of the samples.

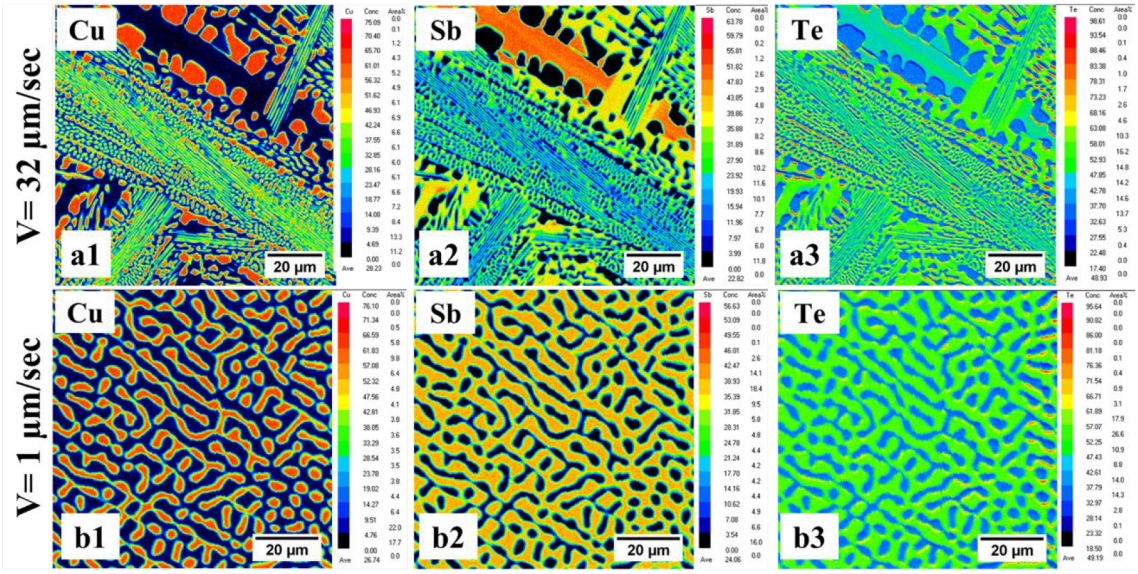

Figure 3. Composition distribution maps (along the transverse section) in parts a1−a3 obtained from the sample solidified at 32 μm/s show the segregation of element Sb in inter colony regions; parts b1−b3 show the composition distribution maps of the sample solidified at 1 μm/s; the maps show the uniform distribution of elements in each phase.

We have also evaluated the percolation of the phases and their connectivity from the observed microstructures. In Figure 2, the clusters are defined as an independent region of the black phase and are labeled using the Hoshen−Kopelman algorithm.[52] The number of clusters per unit area is calculated as the ratio of the total number of black phase clusters in the image to the image size in micrometers. The percolating clusters of the black phase are the ones that extend from one boundary of the image to the opposite boundary. The area fraction of the percolating clusters is the ratio of the total area of the percolating clusters to the image area. The cluster statistics of the images have been provided in Table S1. The

https://doi.org/10.1021/acsaem.1c02664
ACS Appl. Energy Mater. 2021, 4, 11867−11877

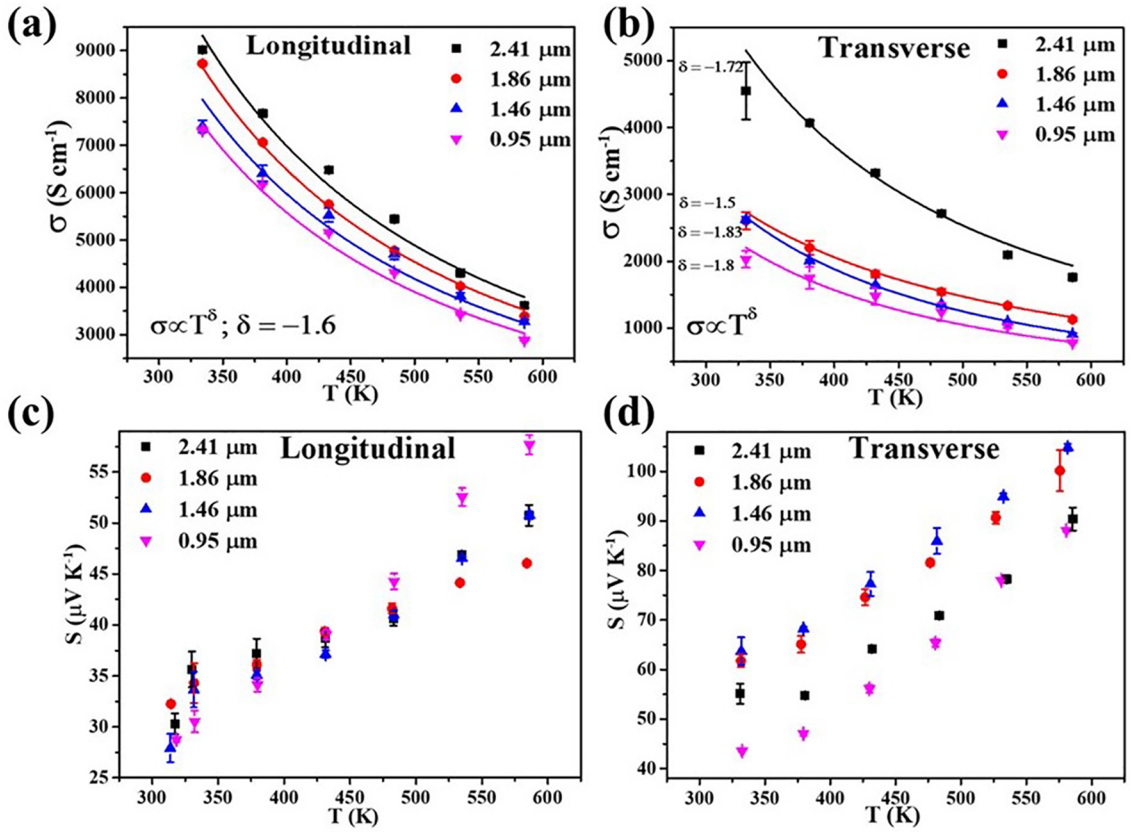

Figure 4. Temperature-dependent variation of the electrical conductivity (σ) and Seebeck coefficient (S) with changes in lamellar spacing; measurement was carried out along the longitudinal (a and c) and transverse directions (b and d).

effect of the clusters and percolating clusters on the electrical transport properties has been discussed in the subsequent section.

3.1.2. Composition Distribution. Composition distribution maps are obtained with an electron probe microanalyzer (JEOL, JXA-8530F) equipped with a field emission source. The elemental map of the sample solidified at 32 μm/s along the transverse direction is shown in Figure 3a1, a2, and a3 for Cu, Sb, and Te, respectively. The higher compositions of Sb in intercolony regions, as shown in Figure 3a2, occur due to Sb segregation in the cell boundary during solidification. Similar variations in Sb composition are also observed in samples solidified at a growth rate of 16 and 4 μm/s (Figures S7 and S8, respectively). The composition distribution map of the sample solidified at 1 μm/s along the transverse section is shown in Figure 3b1, b2, and b3 for Cu, Sb, and Te, respectively. Consistent with the absence of colony regions in the samples solidified at 1 μm/s, we also observe a uniform distribution of elements in their respective phases in these samples.

3.2. Effect of Microstructure on the Thermoelectric Transport Properties. The variation in the rates of solidification also results in a variation of the scale of eutectic microstructure and the morphologies of the phases. As shown in Table 1 and Figure 1c1, the microstructural length scale of the eutectic and the colony spacing decrease with an increase in the solidification rate. The decrease in the length scale will result in enhanced carrier (holes) scattering at the interfaces, affecting transport properties. Moreover, the difference in the alignment of the phases will result in anisotropy of electronic properties in different directions. We have, therefore, measured the transport properties of the alloys in two directions, (1) parallel to the direction of solidification (termed as longitudinal direction) and (2) perpendicular to the direction of solidification (termed as transverse direction), and correlated the properties in each of the directions with the variation in the microstructural length obtained from FFT.

From Figure 4, it can be concluded that the electrical conductivity (σ) of the alloys along the longitudinal direction is higher than that in the transverse directions. It can be understood with the help of the quantitative analysis of SEM microstructures given in Figure 2. With an increase in velocity, the number of clusters per unit area (in both the transverse and the longitudinal directions) increases, which means that the black phase (the higher conducting phase) is less connected. Hence, the electrical conductivity reduces with an increase in the solidification speed. At 1 μm/s, the transverse section has a greater number of clusters per unit area than does its longitudinal counterpart (almost an order of magnitude difference in the number of clusters). As a consequence, σ is also lower in the transverse direction as compared to the longitudinal direction. At 16 μm/s sample, clusters/area values in the transverse and longitudinal sections are almost the same. In both of the samples grown with 1 and 16 μm/s growth rates, percolating clusters are present in the longitudinal section along the growth direction (see Figure 2a3 and b3). But these are absent in the transverse direction (zero percolating clusters in the transverse and from the left boundary to the right boundary in the longitudinal section image). The absence of percolating clusters in the transverse section explains the lower electrical conductivity in this direction. Moreover, as compared to alloys solidified at higher solidification rates, the alloy

https://doi.org/10.1021/acsaem.1c02664
ACS Appl. Energy Mater. 2021, 4, 11867−11877

Table 2. Comparison of the Electrical Conductivity and the Seebeck Coefficient Obtained Using the Parallel Model with That Obtained from Measurements at 350 K

			longitudinal			
			phase fraction		transport properties of composite alloys	
transport properties of bulk	Cu_2Te[38]	Sb_2Te_3[56]	phase 1 Cu_2Te	phase 2 Sb_2Te_3	parallel model (upper limit)	experimental
S (μV K^{-1})	10	100	49	51	40.57	36
σ (S cm^{-1})	10000	5000			746425	7657
κ (W m^{-1} K^{-1})	4.5	2				

Table 3. Comparison of the Electrical Conductivity and the Seebeck Coefficient Obtained Using the Series Model with That Obtained from Measurements at 350 K

			transverse			
			phase fraction		transport properties of composite alloys	
transport properties of bulk	Cu_2Te[38]	Sb_2Te_3[56]	phase 1 Cu_2Te	phase 2 Sb_2Te_3	series model (lower limit)	experimental
S (μV K^{-1})	10	100	41	59	78.52	64
σ (S cm^{-1})	10000	5000			63.03	3898
κ (W m^{-1} K^{-1})	4.5	2				

solidified at 1 μm/s has a more significant number of percolating clusters in the longitudinal direction leading to higher σ.

As shown in Figure 4, the electrical conductivity of the alloys decreases with temperature following the power-law $\sigma \propto T^{\delta}$, where δ is the relaxation time;[53] in both the longitudinal and the transverse directions, the value of δ indicates that acoustic phonon scattering[54−56] dominates the carrier scattering. From the theoretical fit of the power law, the estimated δ values for all of the alloys in the longitudinal direction are ∼1.6. Similar δ values indicate that the scattering phenomena in all alloys are similar in the longitudinal direction. However, the values were different for each alloy in the transverse direction. Such differences in the scattering behavior of each alloy is related to the differences in the nature of the Cu_2Te−Sb_2Te_3 interfaces. This is evidenced through the enhanced electrical conductivity in the transverse direction for a microstructural length scale of 2.41 μm (solidified at 1 μm/s). As compared to the alloys solidified at either 32, 16, or 4 μm/s, which has segregation of Sb in cell boundaries, this alloy has a homogeneous distribution of elements in the respective phases without forming any colonies. Hence, the scattering mechanisms will be remarkably different in this alloy as compared to the other three.

In both measurement directions, the electrical conductivity is higher in the sample with a 1 μm/s solidification rate and decreases systematically with an increase in the rate. It correlates with the systematic decrease in the microstructural length scale λ, as shown in Figure 1c1. As the solidification rate increases, λ decreases from 2.41 to 0.95 μm leading to an increase in the number of interfaces that enhance the charge carriers' scattering. There is a systematic trend between electrical conductivity and the microstructural length scale λ, in both longitudinal and transverse directions; however, the reduction in the conductivity in the transverse direction is significant, almost one-half, as compared to the longitudinal direction. The electrical conductivity in the longitudinal direction is equivalent to an electrical circuit where the resistors (the Cu_2Te/Sb_2Te_3 phases in the eutectics) are connected parallel. In contrast, the same set of resistors (the phases in the eutectic) will have a series connection in the transverse direction.

Following the effective medium theory (EMT) and its generalized derivation (GEMT) (where the interface density is not considered), the electrical conductivity of the composite alloys in both the longitudinal and the transverse directions can be predicted as follows:[57−60]

$$\sigma_{\parallel} = \sigma_1 f_1 + \sigma_2 f_2 \ \text{(parallel model, upper limit)} \tag{1}$$

$$\sigma_{\perp} = \frac{\sigma_1 \sigma_2}{\sigma_2 f_1 + \sigma_1 f_2} \ \text{(series model, lower limit)} \tag{2}$$

where f is the volume fraction, σ is the electrical conductivity, and suffixes 1 and 2 denote the constituent phases. The volume fraction of the phases was calculated using the grid method. The values obtained using relations 1 and 2 are given in Tables 2 and 3, respectively. The comparison has been made at 350 K because the data for all of the parameters are available at this temperature. As can been seen, the experimental values obtained along the longitudinal direction are well below the upper limit predicted by the parallel model; the values obtained along the transverse direction are above the lower limit predicted by the series model. Although the experimental values are within the respective limits, there are large differences between the theoretical and experimental data. The differences arise because in theoretical calculations, we do not consider the interface density that is influenced by the microstructural length scale and the segregation of the phases encountered in the real system.[60]

The Seebeck coefficient of the alloys, measured along the longitudinal and transverse direction, is shown in Figure 4c and d. The alloys exhibit p-type semiconducting nature as reflected in the positive values of the Seebeck coefficients. The following defect equilibrium relations 3 and 4 show the origin of the p-type conductivity. The Cu vacancies (V'_{Cu}) and the antisite defects (Sb'_{Te}) lead to the creation of holes ($h^{\bullet}$) in the pseudobinary alloys.

$$Sb_2Te_3 \rightarrow 2Sb'_{Te} + 2h^{\cdot} + \frac{5}{2}Te_2(g) \tag{3}$$

$$Cu_{2-x}Te \rightarrow 2Cu^{\times}_{Cu} + Te^{\times}_{Te} + xV'_{Cu} + xh^{\cdot} \tag{4}$$

https://doi.org/10.1021/acsaem.1c02664
ACS Appl. Energy Mater. 2021, 4, 11867−11877

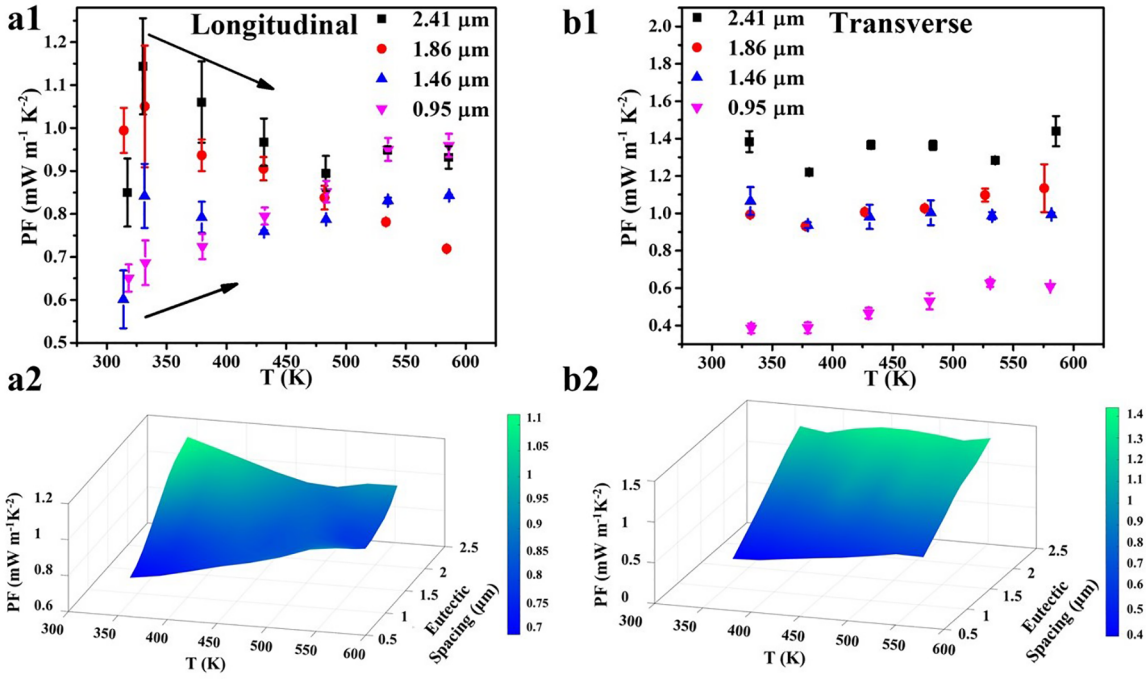

Figure 5. Variation of power factor (PF = $S^2\sigma$) along the (a1) longitudinal direction and the (b1) transverse direction; parts a2 and b2 are the 3D plots showing the entire envelope of PF with variation in temperature as well as lamellar spacing.

The Seebeck coefficients of the composite alloys in both the longitudinal and the transverse directions can be predicted as follows:[57−60]

$$S_{\parallel} = \frac{S_1\sigma_1 f_1 + S_2\sigma_2 f_2}{\sigma_1 f_1 + \sigma_2 f_2} \text{ (parallel model, upper limit)} \quad (5)$$

$$S_{\perp} = \frac{S_1\left(\frac{1}{\kappa_1}\right)f_1 + S_2\left(\frac{1}{\kappa_2}\right)f_2}{\left(\frac{1}{\kappa_1}\right)f_1 + \left(\frac{1}{\kappa_1}\right)f_2} \text{ (series model, lower limit)} \quad (6)$$

where f is the volume fraction, σ is the electrical conductivity, and κ is the thermal conductivity; suffixes 1 and 2 denote the constituent phases; and $S_{\parallel}$ is the upper limit of the Seebeck coefficient in the parallel model and $S_{\perp}$ is the lower limit of the Seebeck coefficient in the series model.

Tables 2 and 3 compare the values obtained from the calculations of $S_{\parallel}$ and $S_{\perp}$ along with those obtained from measurements for the alloy with 2.41 μm at 350 K. The differences between the theoretical prediction and experimental observation might occur because the effect of interface density has not been considered in these models.[60]

It is known that the Seebeck coefficient is influenced by the effective mass and carrier concentration. These two factors are influenced by the sample's homogeneity and defect concentrations (dependent on the sample preparation conditions).[61] In our work, although the starting composition is the same for all of the alloys, the solidification velocities are different, resulting in a microstructure that is nonequilibrium in nature due to the kinetics of mass transport across the moving solid−liquid interface. It is confirmed by the elemental species distribution maps (Figures 3, S8, and S9) that indicate inhomogeneity across the phases for the samples solidified at 32, 16, and 4 μm/s. In contrast, the samples solidified at 1 μm/s show a uniform distribution of elements in the respective phases. Such differences, induced due to processing, resulted in a variation of the Seebeck coefficient in both the longitudinal and the transverse directions of the measurements. It was challenging to carry out high-temperature Hall measurements in these alloys due to the very high carrier concentration ($\sim 10^{21}$ cm^{-3} for Cu_2Te). Hence, we have refrained from discussing the effect of charge carrier concentration on the transport properties in detail. The effect of the microstructural length scale on the electrical conductivity is systematic throughout all of the alloys (Figures 4a and b and S9a and b). It is in contrast to our observation for the Seebeck coefficient. With an increase in the length scale of the multiphase microstructure, the charge carrier scattering at the interfaces will be less, and the value of the Seebeck coefficient will decrease with an increase in microstructural length scale (λ). In the longitudinal direction, the Seebeck values decrease systematically until a λ of 1.86 μm. After that, a slight increase in S can be observed as λ increases to 2.41 μm. In the transverse direction, the Seebeck value for a microstructural length scale λ of 0.95 μm is $\sim$88 μV K^{-1} and exhibits a peak at λ value of 1.46 μm. Thereafter, it decreased systematically from 104 to 90 μV K^{-1} with an increase in the value of λ from 1.46 to 2.41 μm.

The power factor (PF = $S^2\sigma$) for all of the alloys, in both the longitudinal and the transverse directions, is shown in Figure 5a1 and b1, respectively.

The PF has increased with an increase in λ in both directions of the measurement due to the higher electrical conductivity in the coarser microstructure; however, the trend in PF is more dependent on the direction of the measurement than on the scale of the microstructure. From the microstructural analysis, percolating clusters are present along the longitudinal direction, giving rise to higher electrical conductivity than the transverse direction where such clusters are absent. In contrast, a higher PF was obtained along the transverse direction because S and σ are inversely correlated, and the S^2

https://doi.org/10.1021/acsaem.1c02664
ACS Appl. Energy Mater. 2021, 4, 11867−11877

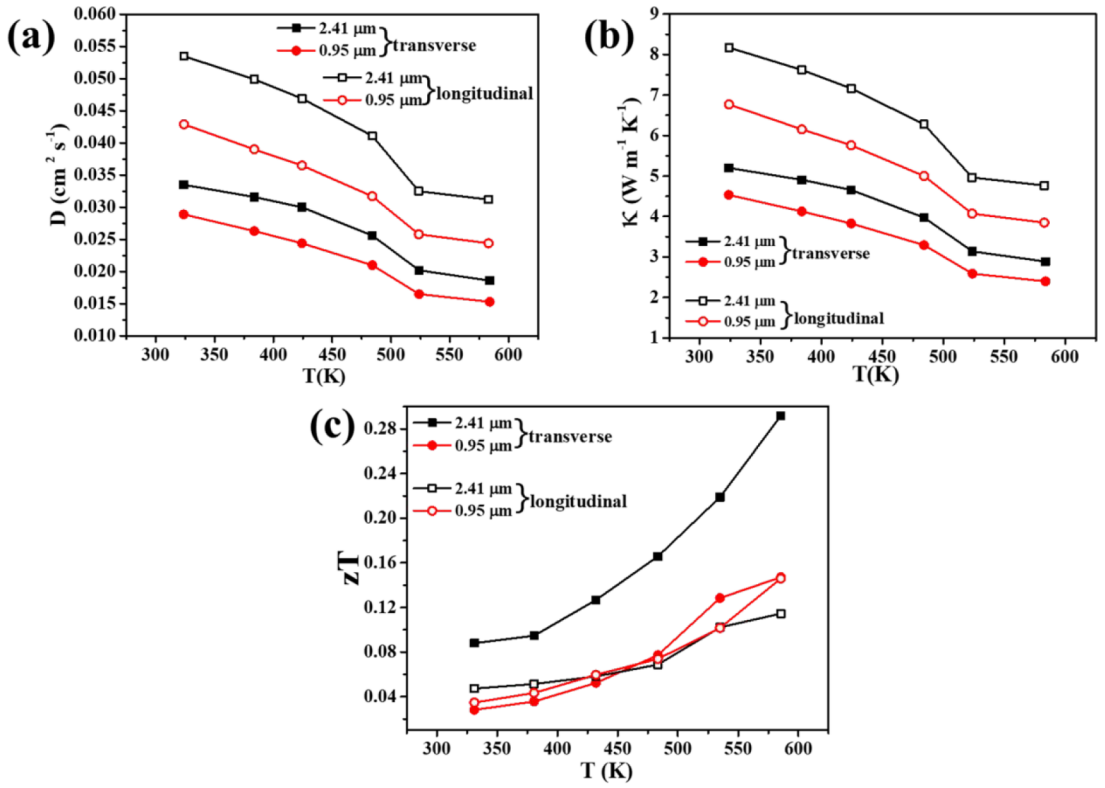

Figure 6. Temperature-dependent variation of (a) thermal diffusivity (D), (b) thermal conductivity (κ), and (c) figure of merit (zT).

term in PF dominates. It can be observed from the microstructural studies that the formation of colonies in the eutectic system could be suppressed by reducing the solidification velocity. Suppression of colonies eliminated the compositional inhomogeneity arising from the segregation of the components in the intercolony regions. Such a uniform microstructure obtained below the critical velocity (i.e., 1 μm/s) showed a uniform distribution of components. It improved the thermoelectric power factor, which was even higher than that obtained in ref 40 for the same eutectic composition. The highest power factor was obtained for the alloy with a λ of 2.41 μm along the transverse direction (Table S2).

We have plotted the data in 3D (in Figure 5a2 and b2) to show the entire envelope of power factors' variation with temperature as well as microstructural length λ. 3D data of longitudinal measurements reveal that the power factor values converge to a range of 0.7−1.0 mW m^{-1} K^{-2} after 450 K, irrespective of the microstructural length scale; however, the corresponding 3D data of transverse measurements show a variation with the length scale λ. The temperature independence in PF arises mainly because the electrical conductivity does not vary significantly over the temperature range of the measurement along the transverse direction, unlike that in the longitudinal direction.

It can be seen from Figure 6a and b that the thermal diffusivity (D) and the thermal conductivity of the alloy solidified at a higher solidification rate (32 μm/s with λ = 0.95 μm) are lower than those of the alloy solidified at a slower rate (1 μm/s with λ = 2.41 μm) in both the transverse as well as the longitudinal directions. As λ decreases from 2.41 to 0.95 μm, the number of interfaces increases leading to enhanced scattering of carriers. More so, the alloys have a lower thermal conductivity along the transverse direction than that in the longitudinal measurement direction. Both of these trends are in good agreement with that observed for electrical conductivity.

A comparison between the figure of merit (zT) of the alloys with λ values of 2.41 and 0.95 μm along both of the directions is shown in Figure 6c. Combined with the low thermal conductivity and a higher power factor, a zT of 0.29 at 580 K was obtained for the alloy with a λ of 2.41 μm along the transverse direction.

Although the thermoelectric community focuses primarily on a high figure of merit to enhance the device efficiency, the efficiency alone is not the only parameter in practical applications.[62−64] The output power density (w) is equally important[22,65] and is given by the relation:

$$w = \frac{1}{4}\frac{(T_H - T_C)}{L}(\mathrm{PF})_{engg} \quad (7)$$

where $(\mathrm{PF})_{engg} = \frac{\left(\int_{T_C}^{T_H} S(T)\,dT\right)^2}{\left(\int_{T_C}^{T_H} \rho(T)\,dT\right)}$ (here, $\rho = 1/\sigma$);[22,54,65,66] L is the length of the thermoelectric leg, and T_H and T_C are the temperatures of the hot and cold sides, respectively. For the given working conditions (i.e., fixed L, length of the leg of the device, and temperature gradient), w is dependent only on the $(\mathrm{PF})_{engg}$. From Figure 7, it can be observed that, similar to the conventional PF, the engineering PF is also higher in the alloy with λ = 2.41 μm along the transverse direction. In the longitudinal direction, however, $(\mathrm{PF})_{engg}$ is similar in the alloys with 2.41 and 0.95 μm spacing. Therefore, the effect of variation in the length scale of microstructure on $(\mathrm{PF})_{engg}$ is more pronounced in the alloys along the transverse direction than that in the longitudinal direction. The difference of output

https://doi.org/10.1021/acsaem.1c02664
ACS Appl. Energy Mater. 2021, 4, 11867−11877

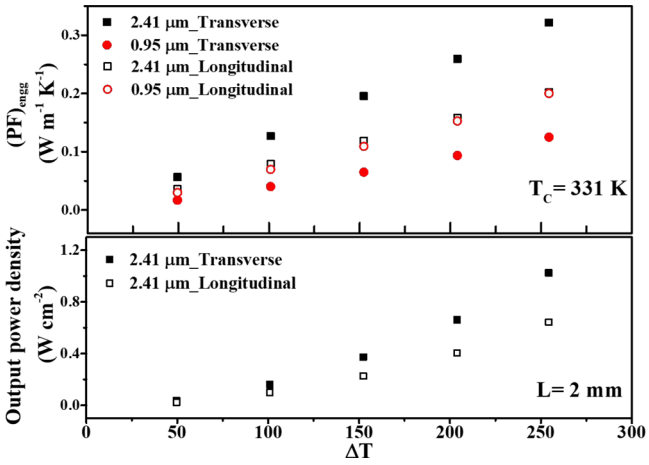

Figure 7. ΔT-dependent $(PF)_{engg}$ of the alloys (with lamellar spacing of 2.41 and 0.95 μm) at T_C = 331 K and output power density of the alloys (for 2.41 μm) in a cubic-shaped TE leg with a leg length of 2 mm along both the longitudinal and the transverse directions.

power density "w" is also plotted as a function of ΔT ($T_H - T_C$) in Figure 7 for an "L" value of 2 mm. At a ΔT of 250 K, a maximum of 1.03 W cm^{-2} could be observed along the transverse direction that is higher by 57% than that observed in the longitudinal direction. Thus, the engineering of the microstructure is an essential component for enhancing the performance of a thermoelectric device.

4. CONCLUSIONS

The present work characterized the arrangement of phases, their microstructural length scale, and the compositions of pseudobinary $(Cu_2Te)_{62.02}-(Sb_2Te_3)_{37.98}$ alloys during controlled growth. The compositional inhomogeneity and segregation at cellular interfaces during higher growth rates are expected to contribute to the charge carrier scattering and the increased interface density. The sample solidified at a slower growth rate (1 μm/s) had uniform microstructures free of cellular segregation. Because of the variation in the configuration of the phases along the longitudinal and transverse directions, anisotropy was observed in the thermoelectric transport properties. In our previous work, the alloys of the pseudobinary system of $(Cu_2Te)_{1-x}-(Sb_2Te_3)_x$ were synthesized via furnace melting and subsequent cooling.[40] Contrary to the directional solidification technique used in this Article, there was no control of the eutectic growth during solidification in the earlier report. The present work permitted us to correlate the scale and arrangements of the multicomponent phases with the thermoelectric power factor. We have quantified the microstructure digitally by measuring the microstructural length scale through Fourier transforms and a cluster base model. It permitted us to correlate the microstructure quantitatively with the thermoelectric transport properties in a set of pseudobinary $Cu_2Te-Sb_2Te_3$ eutectic alloys. The anisotropy in microstructure has been achieved by directional solidification. A decrease in the microstructural length scale λ from 2.41 to 0.95 μm resulted in increased carrier scattering. Hence, the electrical and thermal conductivities were the least in the sample with λ = 0.95 μm in both directions. However, the low electrical conductivity adversely affected the thermoelectric power factor (PF). A maximum value of PF of ~1.4 mW m^{-1} K^{-2} and a higher zT of 0.29 at 580 K could be obtained along the transverse direction in the sample, with λ = 2.41 μm, free of cellular segregation.

Regarding materials' development for thermoelectricity, one focuses primarily on obtaining a high figure of merit to enhance the device efficiency; however, efficiency is not the only parameter of importance in practical applications. The evaluation of output power density (w) is also of crucial importance. We highlighted the effect of microstructure on the thermoelectric transport properties by evaluating the engineering power factor and output power density and how microstructure can be tuned to obtain a better performance. For a ΔT of 250 K, the output power density increased to ~57% from the longitudinal to the transverse directions in the alloy with a lamellar spacing of 2.41 μm. It has an implication in the actual design of the thermoelectric legs, the microstructure of which needs to be controlled for maximum efficiency.

■ ASSOCIATED CONTENT

Supporting Information

The Supporting Information is available free of charge at https://pubs.acs.org/doi/10.1021/acsaem.1c02664.

Pseudobinary phase diagram of $Cu_2Te-Sb_2Te_3$, additional experimental details with a schematic of the experimental setup, micrographs of directionally solidified samples at different velocities from transverse sections at higher magnification, methodology of the measurement of microstructural length scale and colony spacing, SEM and corresponding FFT images of sample solidified at 1 μm/s along the transverse and longitudinal direction, composition distribution maps, powder X-ray diffraction patterns, specific heat capacity, and thermoelectric figure of merit of the alloys (PDF)

■ AUTHOR INFORMATION

Corresponding Authors

Kamanio Chattopadhyay − *Interdisciplinary Centre for Energy Research, Indian Institute of Science, Bangalore 560012, India; Department of Materials Engineering, Indian Institute of Science, Bangalore 560012, India;* orcid.org/0000-0001-9415-2141; Email: kamanio@iisc.ac.in

Shriparna Mukherjee − *Interdisciplinary Centre for Energy Research, Indian Institute of Science, Bangalore 560012, India;* Present Address: Department of Chemistry, University of Reading, Whiteknights, Reading RG6 6DX, United Kingdom; orcid.org/0000-0002-1941-5551; Email: shriparnamuk@alum.iisc.ac.in

Authors

Shanmukha Kiran Aramanda − *Department of Materials Engineering, Indian Institute of Science, Bangalore 560012, India*

Surafel Shiferaw Legese − *Interdisciplinary Centre for Energy Research, Indian Institute of Science, Bangalore 560012, India; Faculty of Materials Science and Engineering, Jimma Institute of Technology, Jimma 378, Ethiopia*

Alexander Riss − *Institute of Solid State Physics, TU Wien, Wien A-1040, Austria*

Gerda Rogl − *Institute of Materials Chemistry, Universität Wien, Wien A-1090, Austria;* orcid.org/0000-0002-8056-5006

Olu Emmanuel Femi − *Faculty of Materials Science and Engineering, Jimma Institute of Technology, Jimma 378, Ethiopia;* orcid.org/0000-0002-6069-7968
Ernst Bauer − *Institute of Solid State Physics, TU Wien, Wien A-1040, Austria*
Peter Franz Rogl − *Institute of Materials Chemistry, Universität Wien, Wien A-1090, Austria;* orcid.org/0000-0002-7733-1612

Complete contact information is available at: https://pubs.acs.org/10.1021/acsaem.1c02664

Author Contributions

S.M., S.K.A., and O.E.F. designed the research; S.M., S.K.A., and S.S.L. performed the research; S.S.L. weighed the respective metals and carried out induction melting; S.K.A. conducted the directional solidification of the alloys; S.M. and S.K.A. performed the microstructure characterizations; S.M. measured the Seebeck coefficient and electrical conductivity; A.R. and G.R. measured the thermal diffusivity and specific heat capacities; S.M., S.K.A., and O.E.F. prepared the manuscript; G.R., P.F.R., and E.B. revised the manuscript; and K.C. supervised the work and revised the manuscript.

Author Contributions

[#]S.M. and S.K.A. contributed equally.

Notes

The authors declare no competing financial interest.

■ ACKNOWLEDGMENTS

We would like to acknowledge the microscopy facilities (EPMA and SEM) available at the Advanced Facility for Microscopy and Microanalysis (AFMM) and at the Department of Materials Engineering, Indian Institute of Science, Bangalore. S.S.L. is grateful to the Jimma Institute of Technology, Jimma, Ethiopia, for a Master scholarship and to the Office of International Relation (OIR), Indian Institute of Science, for support. O.E.F. would also like to acknowledge the Office of International Relations (OIR), IISc, Bangalore, India, for accommodation support and the ExiST project at the JiT Center of Excellence funded by kFW of Germany for their support. We would like to thank Prof. Abhik Choudhury, Department of Materials Engineering, Indian Institute of Science, Bangalore, India, for extending the facility for directional solidification. We would also like to thank Mr. Sumeeth Khanna and Prof. Abhik Choudhury for helping us with the cluster model image analysis and for insightful discussions.

■ REFERENCES

(1) Gorsse, S.; Bauer Pereira, P.; Decourt, R.; Sellier, E. Microstructure Engineering Design for Thermoelectric Materials: An Approach to Minimize Thermal Diffusivity. *Chem. Mater.* **2010**, *22* (3), 988−993.
(2) Cui, J. L.; Xue, H. F.; Xiu, W. J. Microstructures and Thermoelectric Properties of P-Type Pseudo-Binary $Ag_xBi_{0.5}Sb_{1.5-x}Te_3$ (x = 0.05−0.4) Alloys Prepared by Cold Pressing. *Mater. Lett.* **2006**, *60* (29−30), 3669−3672.
(3) Femi, O. E.; Ravishankar, N.; Chattopadhyay, K. Microstructure Evolution and Thermoelectric Properties of Te-Poor and Te-Rich $(Bi,Sb)_2Te_3$ Prepared via Solidification. *J. Mater. Sci.* **2016**, *51* (15), 7254−7265.
(4) Mori, T. Novel Principles and Nanostructuring Methods for Enhanced Thermoelectrics. *Small* **2017**, *13* (45), 1−10.
(5) Zhang, Y.; Wu, L.; Zhang, J.; Xing, J.; Luo, J. Eutectic Microstructures and Thermoelectric Properties of MnTe-Rich Precipitates Hardened PbTe. *Acta Mater.* **2016**, *111*, 202−209.
(6) Meng, X.; Liu, Z.; Cui, B.; Qin, D.; Geng, H.; Cai, W.; Fu, L.; He, J.; Ren, Z.; Sui, J. Grain Boundary Engineering for Achieving High Thermoelectric Performance in N-Type Skutterudites. *Adv. Energy Mater.* **2017**, *7* (13), 1602582.
(7) Snyder, G. J.; Toberer, E. S. Complex Thermoelectric Materials. *Nat. Mater.* **2008**, *7*, 105−114.
(8) Suk, M.-J.; Choi, G.-H.; Moon, I.-H. Determination of Microstructural Anisotropy in Sb-InSb Eutectic by Electrical Resistivity Measurement. *J. Mater. Sci.* **1996**, *31* (6), 1663−1668.
(9) Liu, D.; Dreßler, C.; Seyring, M.; Teichert, S.; Rettenmayr, M. Reduced Thermal Conductivity of Bi-In-Te Thermoelectric Alloys in a Eutectic Lamellar Structure. *J. Alloys Compd.* **2018**, *748*, 730−736.
(10) Gelbstein, Y.; Dado, B.; Ben-Yehuda, O.; Sadia, Y.; Dashevsky, Z.; Dariel, M. P. High Thermoelectric Figure of Merit and Nanostructuring in Bulk P-Type $Ge_x(Sn_yPb_{1-y})_{1-x}Te$ Alloys Following a Spinodal Decomposition Reaction. *Chem. Mater.* **2010**, *22* (3), 1054−1058.
(11) Zhang, Q.; Chere, E. K.; Wang, Y.; Kim, H. S.; He, R.; Cao, F.; Dahal, K.; Broido, D.; Chen, G.; Ren, Z. High Thermoelectric Performance of N-Type $PbTe_{1-y}S_y$ Due to Deep Lying States Induced by Indium Doping and Spinodal Decomposition. *Nano Energy* **2016**, *22*, 572−582.
(12) Sugar, J. D.; Medlin, D. L. Precipitation of Ag_2Te in the Thermoelectric Material $AgSbTe_2$. *J. Alloys Compd.* **2009**, *478* (1−2), 75−82.
(13) Yu, C.; Xie, H.; Fu, C.; Zhu, T.; Zhao, X. High Performance Half-Heusler Thermoelectric Materials with Refined Grains and Nanoscale Precipitates. *J. Mater. Res.* **2012**, *27* (19), 2457−2465.
(14) Xie, H.; Su, X.; Yan, Y.; Liu, W.; Chen, L.; Fu, J.; Yang, J.; Uher, C.; Tang, X. Thermoelectric Performance of $CuFeS_{2+2x}$ Composites Prepared by Rapid Thermal Explosion. *NPG Asia Mater.* **2017**, *9*, 1−12.
(15) Xie, H.-H.; Yu, C.; Zhu, T.-J.; Fu, C.-G.; Snyder, G. J.; Zhao, X.-B. Increased Electrical Conductivity in Fine- Grained (Zr, Hf) NiSn Based Thermoelectric Materials with Nanoscale Precipitates. *Appl. Phys. Lett.* **2012**, *100* (254104), 1−4.
(16) Chalmers, B. Principles of Solidification. *Applied Solid State Physics*; Springer: New York, 1964; pp 161−170.
(17) Dantzig, J. A.; Rappaz, M. *Solidification*, 2nd ed.; EPFL Press: Switzerland, 2016.
(18) Ikeda, T.; Ravi, V. A.; Jeffrey Snyder, G. Microstructure Size Control through Cooling Rate in Thermoelectric $PbTe-Sb_2Te_3$ Composites. *Metall. Mater. Trans. A* **2010**, *41*, 641−650.
(19) Ikeda, T.; Collins, L. A.; Ravi, V. A.; Gascoin, F. S.; Haile, S. M.; Snyder, G. J. Self-Assembled Nanometer Lamellae of Thermoelectric PbTe and SbTe with Epitaxy-like Interfaces Self-Assembled Nanometer Lamellae of Thermoelectric PbTe and Sb_2Te_3 with Epitaxy-like Interfaces. *Chem. Mater.* **2007**, *19* (4), 763−767.
(20) Sootsman, J. R.; He, J.; Dravid, V. P.; Li, C. P.; Uher, C.; Kanatzidis, M. G. High Thermoelectric Figure of Merit and Improved Mechanical Properties in Melt Quenched PbTe-Ge and $PbTe-Ge_{1-x}Si_x$ Eutectic and Hypereutectic Composites. *J. Appl. Phys.* **2009**, *105*, 083718.
(21) Mori, T. Novel Principles and Nanostructuring Methods for Enhanced Thermoelectrics. *Small* **2017**, *13* (45), 1−10.
(22) Liu, W.; Kim, H. S.; Jie, Q.; Ren, Z. Importance of High Power Factor in Thermoelectric Materials for Power Generation Application: A Perspective. *Scr. Mater.* **2016**, *111*, 3−9.
(23) Vaney, J. B.; Aminorroaya Yamini, S.; Takaki, H.; Kobayashi, K.; Kobayashi, N.; Mori, T. Magnetism-Mediated Thermoelectric Performance of the Cr-Doped Bismuth Telluride Tetradymite. *Mater. Today Phys.* **2019**, *9*, 100090.
(24) Kulkarni, A. A.; Hanson, E.; Zhang, R.; Thornton, K.; Braun, P. V. Archimedean Lattices Emerge in Template-Directed Eutectic Solidification. *Nature* **2020**, *577* (7790), 355−358.

(25) Pawlak, D. A.; Turczynski, S.; Gajc, M.; Kolodziejak, K.; Diduszko, R.; Rozniatowski, K.; Smalc, J.; Vendik, I. How Far Are We from Making Metamaterials by Self-Organization? The Microstructure of Highly Anisotropic Particles with an SRR-like Geometry. *Adv. Funct. Mater.* **2010**, *20*, 1116−1124.
(26) Galasso, F. S. Unidirectionally Solidified Eutectics for Optical, Electronic, and Magnetic Applications. *JOM* **1967**, *19* (6), 17−21.
(27) Chadwick, G. A. Structure and Properties of Eutectic Alloys. *Met. Sci.* **1975**, *9* (1), 300−304.
(28) Osewski, P.; Belardini, A.; Centini, M.; Valagiannopoulos, C.; Leahu, G.; Li Voti, R.; Tomczyk, M.; Alù, A.; Pawlak, D. A.; Sibilia, C. New Self-Organization Route to Tunable Narrowband Optical Filters and Polarizers Demonstrated with ZnO−$ZnWO_4$ Eutectic Composite. *Adv. Opt. Mater.* **2020**, *1901617*, 1−10.
(29) Chung, J.; Hyon, J.; Park, K. S.; Cho, B.; Baek, J.; Kim, J.; Lee, S. U.; Sung, M. M.; Kang, Y. Controlled Growth of Rubrene Nanowires by Eutectic Melt Crystallization. *Sci. Rep.* **2016**, *6* (March), 1−11.
(30) Chadwick, G. A. Yield Poixt Analyses in Eutectic. *Acta Metall.* **1976**, *24*, 1137−1146.
(31) Bei, H.; Pharr, G. M.; George, E. P. A Review of Directionally Solidified Intermetaliic Composites for High-Temperature Structural Applications. *J. Mater. Sci.* **2004**, *39* (12), 3975−3984.
(32) Yoon, G.; Kim, I.; Rho, J. Challenges in Fabrication towards Realization of Practical Metamaterials. *Microelectron. Eng.* **2016**, *163*, 7−20.
(33) Elliot, R. *Eutectic Solidification Processing: Crystalline and Glassy Alloys*; Elsevier: New York, 1983.
(34) Akamatsu, S.; Plapp, M. Eutectic and Peritectic Solidification Patterns. *Curr. Opin. Solid State Mater. Sci.* **2016**, *20* (1), 46−54.
(35) Kuliev, R. A.; Krestovnikov, A. N.; Glazov, V. M. Phase Equilibria and Intermolecular Interactions in Systems Formed by Copper and Antimony Chalcogenides *Russ. J. Phys. Chem.* **1969**.
(36) Mukherjee, S.; Parasuraman, R.; Umarji, A. M.; Rogl, G.; Rogl, P.; Chattopadhyay, K. Effect of Fe Alloying on the Thermoelectric Performance of Cu_2Te. *J. Alloys Compd.* **2020**, *817* (152729), 1−11.
(37) Zhao, K.; Liu, K.; Yue, Z.; Wang, Y.; Song, Q.; Li, J.; Guan, M.; Xu, Q.; Qiu, P.; Zhu, H.; Chen, L.; Shi, X. Are Cu_2Te-Based Compounds Excellent Thermoelectric Materials? *Adv. Mater.* **2019**, *1903480*, 1−8.
(38) Ballikaya, S.; Chi, H.; Salvador, J. R.; Uher, C. Thermoelectric Properties of Ag-Doped Cu_2Se and Cu_2Te. *J. Mater. Chem. A* **2013**, *1* (40), 12478.
(39) He, Y.; Zhang, T.; Shi, X.; Wei, S.-H.; Chen, L. High Thermoelectric Performance in Copper Telluride. *NPG Asia Mater.* **2015**, *7* (8), e210.
(40) Mukherjee, S.; Femi, O. E.; Chetty, R.; Chattopadhyay, K.; Suwas, S.; Mallik, R. C. Microstructure and Thermoelectric Properties of Cu_2Te-Sb_2Te_3 pseudo-Binary System. *Appl. Surf. Sci.* **2018**, *449*, 805−814.
(41) Venkatasubramanian, R.; Siivola, E.; Colpitts, T.; O'Quinn, B. Thin-Film Thermoelectric Devices with High Room-Temperature Figures of Merit. *Nature* **2001**, *413*, 597−602.
(42) Zhang, Y.; Sa, B.; Zhou, J.; Sun, Z. First Principles Investigation of the Structure and Electronic Properties of Cu_2Te. *Comput. Mater. Sci.* **2014**, *81*, 163−169.
(43) Mukherjee, S.; Chetty, R.; Madduri, P. V. P.; Nayak, A. K.; Wojciechowski, K.; Ghosh, T.; Chattopadhyay, K.; Suwas, S.; Mallik, R. C. Investigation on the Structure and Thermoelectric Properties of Cu_xTe Binary Compounds. *Dalt. Trans.* **2019**, *48* (3), 1040−1050.
(44) Liu, H.; Shi, X.; Xu, F.; Zhang, L.; Zhang, W.; Chen, L.; Li, Q.; Uher, C.; Day, T.; Snyder, G. J. Copper Ion Liquid-like Thermoelectrics. *Nat. Mater.* **2012**, *11* (5), 422−425.
(45) Nithiyanantham, U.; Ede, S. R.; Ozaydin, M. F.; Liang, H.; Rathishkumar, A.; Kundu, S. Low Temperature, Shape-Selective Formation of Sb_2Te_3 Nanomaterials and Their Thermoelectric Applications. *RSC Adv.* **2015**, *5* (109), 89621−89634.
(46) Aramanda, S. K.; Salapaka, S. K.; Khanna, S.; Chattopadhyay, K.; Choudhury, A. Exotic Colony Formation in Sn-Te Eutectic System. *Acta Mater.* **2020**, *197*, 108−121.
(47) Aramanda, S. K.; Khanna, S.; Salapaka, S. K.; Chattopadhyay, K.; Choudhury, A. Crystallographic and Morphological Evidence of Solid−Solid Interfacial Energy Anisotropy in the Sn-Zn Eutectic System. *Metall. Mater. Trans. A* **2020**, *51* (12), 6387−6405.
(48) Mullins, W. W.; Sekerka, R. F. Stability of a Planar Interface during Solidification of a Dilute Binary Alloy. *J. Appl. Phys.* **1964**, *35* (2), 444−451.
(49) Akamatsu, S.; Faivre, G. Traveling Waves, Two-Phase Fingers, and Eutectic Colonies in Thin-Sample Directional Solidification of a Ternary Eutectic Alloy. *Phys. Rev. E: Stat. Phys., Plasmas, Fluids, Relat. Interdiscip. Top.* **2000**, *61* (4), 3757−3770.
(50) Akamatsu, S.; Perrut, M.; Bottin-Rousseau, S.; Faivre, G. Spiral Two-Phase Dendrites. *Phys. Rev. Lett.* **2010**, *104* (5), 1−4.
(51) Jackson, K. A.; Hunt, J. D. Lamellar and Rod Eutectic Growth. *Dyn. Curved Front.* **1988**, *236*, 363−376.
(52) Hoshen, J.; Kopelman, R. Percolation and Cluster Distribution. I. Cluster Multiple Labeling Technique and Critical Concentration Algorithm. *Phys. Rev. B* **1976**, *14* (8), 3438−3445.
(53) Ovadyahu, Z.; Imry, Y. Conductivity Power-Law Temperature Dependence of Thin Indium Oxide Films. *J. Phys. C: Solid State Phys.* **1985**, *18* (1), 18−25.
(54) Shuai, J.; Mao, J.; Song, S.; Zhu, Q.; Sun, J.; Wang, Y.; He, R.; Zhou, J.; Chen, G.; Singh, D. J.; Ren, Z. Tuning the Carrier Scattering Mechanism to Effectively Improve the Thermoelectric Properties. *Energy Environ. Sci.* **2017**, *10* (3), 799−807.
(55) Sarkar, S.; Zhang, X.; Hao, S.; Hua, X.; Bailey, T. P.; Uher, C.; Wolverton, C.; Dravid, V. P.; Kanatzidis, M. G. Dual Alloying Strategy to Achieve a High Thermoelectric Figure of Merit and Lattice Hardening in P-Type Nanostructured PbTe. *ACS Energy Lett.* **2018**, *3* (10), 2593−2601.
(56) Ibrahim, M. M.; Wakkad, M. M.; Shokr, E. K.; Ei-ghani, H. A. A. Electrical Properties of Antimony Telluride. *Appl. Phys. A: Solids Surf.* **1991**, *52*, 237−241.
(57) Ashby, M. F.; Brechet, Y. J. Designing Hybrid Materials. *Acta Mater.* **2003**, *51*, 5801−5821.
(58) Wang, M.; Pan, N. Predictions of Effective Physical Properties of Complex Multiphase Materials. *Mater. Sci. Eng., R* **2008**, *63* (1), 1−30.
(59) Zhang, B.; Sun, J.; Katz, H. E.; Fang, F.; Opila, R. L. Promising Thermoelectric Properties of Commercial PEDOT:PSS Materials and Their Bi_2Te_3 Powder Composites. *ACS Appl. Mater. Interfaces* **2010**, *2* (11), 3170−3178.
(60) Liu, D.; Li, X.; De Castro Borlido, P. M.; Botti, S.; Schmechel, R.; Rettenmayr, M. Anisotropic Layered Bi_2Te_3 -In_2Te_3 Composites: Control of Interface Density for Tuning of Thermoelectric Properties. *Sci. Rep.* **2017**, *7* (January), 1−13.
(61) Ikeda, T.; Iwanaga, S.; Wu, H. J.; Marolf, N. J.; Chen, S. W.; Snyder, G. J. A Combinatorial Approach to Microstructure and Thermopower of Bulk Thermoelectric Materials: The Pseudo-Ternary PbTe-Ag_2Te-Sb_2Te_3 System. *J. Mater. Chem.* **2012**, *22* (46), 24335−24347.
(62) Ryu, B.; Chung, J.; Choi, E.-A.; Ziolkowski, P.; Müller, E.; Park, S. Counterintuitive Example on Relation between ZT and Thermoelectric Efficiency. *Appl. Phys. Lett.* **2020**, *116* (19), 193903.
(63) Narducci, D. Do We Really Need High Thermoelectric Figures of Merit? A Critical Appraisal to the Power Conversion Efficiency of Thermoelectric Materials. *Appl. Phys. Lett.* **2011**, *99* (10), 102104.
(64) Wolf, M.; Hinterding, R.; Feldhoff, A. High Power Factor vs. High ZT-A Review of Thermoelectric Materials for High-Temperature Application. *Entropy* **2019**, *21* (11), 1058.
(65) Kim, H. S.; Liu, W.; Chen, G.; Chu, C. W.; Ren, Z. Relationship between Thermoelectric Figure of Merit and Energy Conversion Efficiency. *Proc. Natl. Acad. Sci. U. S. A.* **2015**, *112* (27), 8205−8210.
(66) Kim, H. S.; Liu, W.; Ren, Z. Bridge between the Materials and Devices of Thermoelectric Power Generators. *Energy Environ. Sci.* **2017**, *10* (1), 69−85.

https://doi.org/10.1021/acsaem.1c02664
ACS Appl. Energy Mater. 2021, 4, 11867−11877